Supporting information

Modulating the electronic structure of Ni(OH)$_2$ by coupling with low-content Pt for boosting urea oxidation reaction enables significantly promoted energy-saving hydrogen production

Mengxiao Zhong,[a] Meijiao Xu,[a] Siyu Ren,[a] Weimo Li,[a] Ce Wang,[a] Mingbin Gao,*[b] Xiaofeng Lu*[a]

[a]Alan G. MacDiarmid Institute, College of Chemistry, Jilin University, 2699 Qianjin Street, Changchun 130012, P. R. China.

[b]National Engineering Research Center of Lower-Carbon Catalysis Technology, Dalian National Laboratory for Clean Energy, Dalian Institute of Chemical Physics, Chinese Academy of Sciences, Dalian 116023, P. R. China.

*Corresponding authors. Email: mbgao@dicp.ac.cn (Dr. M. Gao); xflu@jlu.edu.cn (Prof. X. Lu)

Experiment section

Chemicals and reagents

Polyacrylonitrile (PAN, M_w = 80,000) and N, N-dimethylformamide (DMF) were purchased from Jilin Chemical Plant and Tianjin Tiantai Fine Chemicals Co. Ltd., respectively. Nickel(II) acetate tetrahydrate (Ni(CH$_3$COO)$_2$·4H$_2$O) was obtained from Sinopharm Chemical Reagent Co. Ltd. Nickel nitrate hexahydrate (Ni(NO$_3$)$_2$·6H$_2$O) was bought from Beijing Chemical Works. Chloroplatinic acid hexahydrate (H$_2$PtCl$_6$·6H$_2$O) was provided by Aladdin. Commercial Pt/C (20 wt%) and Nafion solution (5 %) were available from Johnson Matthey and Sigma-Aldrich, respectively.

Fabrication of Ni-CNFs

Firstly, 0.30 g of PAN was added into DMF to form a polymer solution (5.5 wt%),

followed by adding 0.45 g of Ni(CH$_3$COO)$_2$·4H$_2$O under continuous stirring. Then, the obtained homogeneous precursor was placed in a syringe under an electric field with a high voltage of 16 kV for electrospinning. Subsequently, the green Ni precursor-PAN membranes were pre-oxidized at 240 °C for 2 h and then completely carbonized at 800 °C for 2 h in Ar atmosphere. The flexible black Ni-CNFs membrane was finally obtained.

Fabrication of Pt-Ni(OH)$_2$@Ni-CNFs

The final catalysts were obtained through a typical electrodeposition strategy in a three-electrode system, in which the above Ni-CNFs membrane (1 cm × 1 cm), saturated calomel electrode (SCE) and graphite rod were served as working electrode, reference electrode and counter electrode, respectively. The electrodeposition process was carried out at a current density of about 2 mA cm^{-2} for 400 s. Then, the resulting products were washed several times with water and ethanol, and dried in an oven at 45 ºC. Notably, two types of electrolytes were used for the deposition process, which were named as solution A and B, respectively. In detail, the solution A includes 20 mL of aqueous solution with 15 mM Ni(NO$_3$)$_2$ and varied concentrations of H$_2$PtCl$_6$ (0, 1.25, 2.5 and 3.75 mM). Correspondingly, the obtained samples were denoted as Ni(OH)$_2$@Ni-CNFs, Pt-Ni(OH)$_2$@Ni-CNFs-1, Pt-Ni(OH)$_2$@Ni-CNFs-2 and Pt-Ni(OH)$_2$@Ni-CNFs-3, respectively. On the other hand, the solution B was 20 mL of aqueous solution containing different concentrations of H$_2$PtCl$_6$ (1.25, 2.5 and 3.75 mM). And the different samples were correspondingly named as Pt@Ni-CNFs-1, Pt@Ni-CNFs-2 and Pt@Ni-CNFs-3, respectively.

Characterizations

The morphological characteristics of the prepared samples were studied by field emission scanning electron microscopy (FESEM, Thermo Fisher Scientific) and transmission electron microscopy (TEM, JEOL JEM-2100). The FEI Tecnai G2 F20 electron microscope was used to perform the high-resolution transmission electron microscopy (HRTEM) images, energy dispersive X-ray (EDX) patterns and elemental mapping analyses of Pt-Ni(OH)$_2$@Ni-CNFs and the Pt@Ni-CNFs. The crystal type of

the prepared samples was conducted through X-ray diffraction (XRD) analysis by using PANalytical B.V. Empyream. X-ray photoelectron spectra (XPS) were recorded on the Thermo Fisher 250xi spectrometer. Inductively coupled plasma optical emission spectroscopy (ICP-OES) measurement (Agilent 725) was carried out to estimate the weight percentage of Pt in the catalyst. Raman spectra of the powders were collected on LabRAM HR Evolution measurement and the in situ Raman spectra were recorded with an inverted Raman spectroscopy system, which combines a PI spectrometer (PIX2560-SF-Q), 532 nm laser (MSL-III-532nm-100Mw-19021075) and Olympus inverted microscope (IX73).

Electrochemical measurements

All electrochemical experiments were performed on a CHI 760E electrochemical workstation at room temperature. A typical three-electrode system was used for all the half reactions in the experiments, where the catalyst-coated carbon paper (0.4 cm × 0.5 cm) and the calibrated Hg/HgO electrode were served as the working electrode and reference electrode, respectively. In addition, the graphite rod was used as counter electrode for cathodic HER, while Pt wire was used for the anodic OER and UOR reactions. The electrolytes varied depending on the different reactions, where both HER and OER tests were performed in 1 M KOH and the UOR was measured in 1 M KOH/0.33 M urea. To prepare working electrode, 4 mg of catalyst was added into 1 mL of ethanol containing 20 μL of Nafion, and dispersed for at least 30 min to form a uniform catalyst ink. Then, 50 μL of prepared ink was dropped on the carbon paper with a mass loading of 1 mg cm^{-2}. Polarization curves were measured using linear scanning voltammetry (LSV) method with a scan rate of 2 mV s^{-1}, before that, cyclic voltammetry (CV) method was used to activate and stabilize the working electrode. Electrochemical impedance spectroscopy (EIS) test for HER was conducted at an initial potential of -1.1 V vs. Hg/HgO electrode in a frequency range of 10^5-10^{-1} Hz. The OER measurement is carried out in 1 M KOH and the UOR process is conducted in the 1 M KOH/0.15 M urea system. Unless otherwise specified, the polarization curves were corrected for 100 % iR-compensation according to the following equation: E$_{correction}$ =

$E_{experiment}$ - iR_s. The i-t tests for HER and UOR were conducted using the three-electrode configuration, where the catalyst-coated carbon papers were served as the working electrodes (0.4 cm × 0.5 cm, catalyst mass loading of 2 mg cm^{-2}).

The overall water splitting and urea-assisted water splitting measurements were tested using two-electrode configuration, in which the carbon papers coated with Pt-Ni(OH)$_2$@Ni-CNFs and the Pt@Ni-CNFs (0.4 cm × 0.5 cm) were served as anode and cathode with mass loading of 2 mg cm^{-2}, respectively. The electrolyte was set to 1 M KOH and 1 M KOH/0.33 M urea for overall water splitting and urea-assisted water splitting, respectively. Moreover, the stability of the Pt-Ni(OH)$_2$@Ni-CNFs‖Pt@Ni-CNFs electrolyzer was also tested at a constant voltage.

Calibration of Hg/HgO electrode

The Hg/HgO electrode was calibrated by a relatively steady state chronoamperometry method in H$_2$-saturated 1 M KOH. Two polished Pt foils with the same area were served as working electrode and counter electrode to form a three-electrode system. A series of chronoamperometry curves were measured for 300 s to get the current interconvert between the hydrogen oxidation and hydrogen evolution reaction. The potential at zero net current was obtained from the figure plotting the currents at 300 s with the corresponding applied potentials. Herein, the potential of zero net current was shown at -0.922 V vs. Hg/HgO (Fig. S28). Therefore, the potentials were converted to reversible hydrogen electrode (RHE) via the Nernst equation: E_{RHE} = $E_{Hg/HgO}$ + 0.922 V.

Electrochemical calculation methods

Electrochemical surface area (ECSA) was calculated from the double layer capacitance (C$_{dl}$) through a CV method. Specifically, the CV measurements were conducted at different scan rates in a potential range of 0.1-0.2 V vs. Hg/HgO electrode (no Faradic responses). Then, the values of C$_{dl}$ were calculated by plotting capacitive current density Δj (j_{anode} - $j_{cathode}$, acquired from the corresponding CV curves in Fig. S15) at 0.15 V vs. Hg/HgO electrode versus scan rate, and the linear slope value is twice that of the C$_{dl}$. Therefore, the ECSA values were calculated based on the

following equation: ECSA = $(C_{dl} \cdot S)/C_s$, where S is the geometric area of the working electrode and C_s is the specific capacitance of a smooth surface (generally assumed to be 0.04 mF cm^{-2}). Turnover frequency (TOF) was evaluated by the following equation: TOF = $(j \times N_A)/(n \times F \times \Gamma)$, where j is the current density at a certain potential (A cm^{-2}), N_A is the Avogadro constant, n is the number of electron transfers required to generate one molecule of the target product (2 for H_2, 6 for N_2 and CO_2), F is the Faradic constant (96500 C mol^{-1}) and Γ is the surface concentration of the active site or the number of atoms participating in the catalytic reaction. Here, the total metal is considered as the active sites, which is determined from the ICP results. According to the Faraday's law, the power consumption for a water electrolysis process can be expressed as follows:[1]

$$Energy\ consumption,\ kWh\ m^{-3} = V_{cell} \times \frac{nF}{3600} \times \frac{1}{V_m}$$

where the V_{cell} is the voltage during electrolysis, n is the number of electrons (2 for HER), F represents the Faraday constant of 96,500 C mol^{-1}, and V_m is the molar volume of gas to be 24.47 L mol^{-1} at 25 °C and 1 atm.

DFT calculation methods.

All density functional theory (DFT) calculations were performed using the plane-wave pseudopotential method, with the CASTEP module implemented in Material Studio 6.0.[2] The Generalized Gradient Approximation (GGA) with Perdew-Burke-Ernzerhof (PBE) exchange-correlation functional was used to describe the exchange-correlation effects.[3,4] We used plane wave basis with a cut-off energy of 300 eV, self-consistent field (SCF) tolerance of 2×10^{-6} eV, energy 2×10^{-5} eV per atom, maximum force 0.05 eV per Å, maximum stress 0.1 GPa and maximum displacement 0.002 Å, respectively, for the geometry optimization. All atoms were relaxed for the optimization. For the transition state search, the complete LST/QST method was employed. The spin-polarization was considered and used formal spin as initial. The van der Waals correction was also considered in the calculations. Pt$_{20}$ clusters were used to mimic Pt NPs loaded on the Ni(OH)$_2$ surface for UOR. The size of the supercell was (18.42 × 18.42 × 23.20) Å. A vacuum space of 15 Å in the z-direction was set to

minimize interactions among neighboring substrate images. The typical UOR pathway as: $* + CO(NH_2)_2 \rightarrow *CO(NH_2)_2 \rightarrow *CONHNH_2 \rightarrow *CONNH_2 \rightarrow *CONNH \rightarrow *CO(N_2) \rightarrow *CO \rightarrow *CO(OH) \rightarrow *CO_2 \rightarrow * + CO_2$ (g), where * represents the active site.[5-7] Moreover, Pt_{20} clusters were used to mimic Pt nanoparticles loaded on the Ni(111) surface for HER.
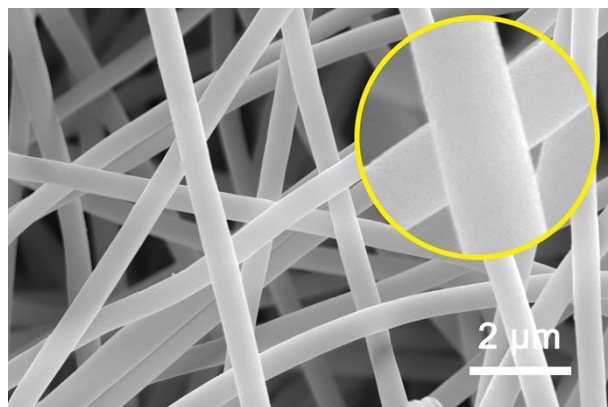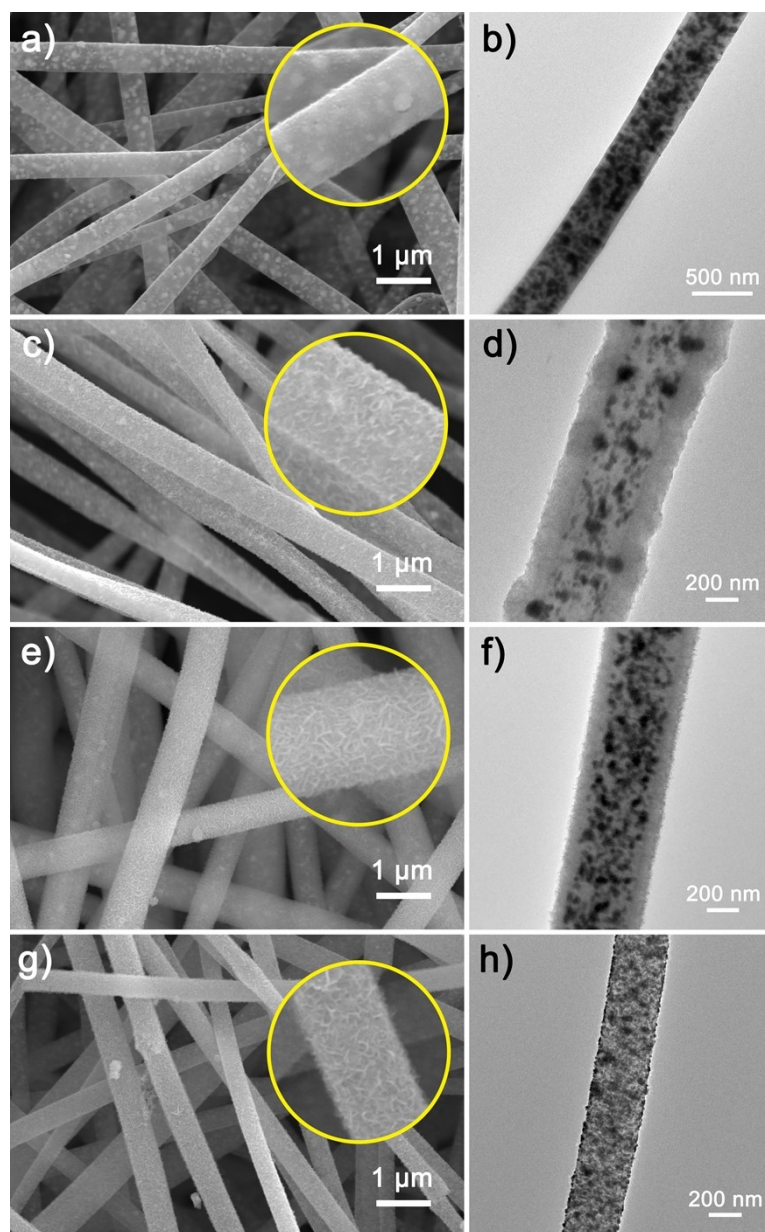
Fig. S1 SEM image of Ni precursor-PAN nanofibers.

Fig. S2 SEM and TEM images of (a) and (b) Ni-CNFs, (c) and (d) Ni(OH)$_2$@Ni-CNFs, (e) and (f) Pt-Ni(OH)$_2$@Ni-CNFs-1, (g) and (h) Pt-Ni(OH)$_2$@Ni-CNFs-3.
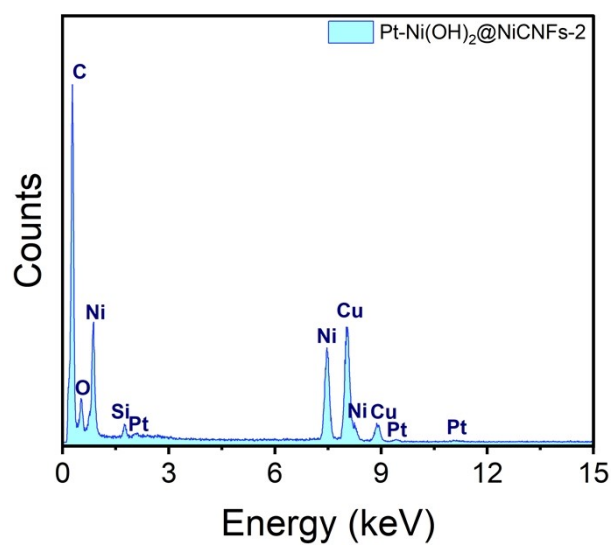
Fig. S3 EDX pattern of Pt-Ni(OH)$_2$@Ni-CNFs-2.
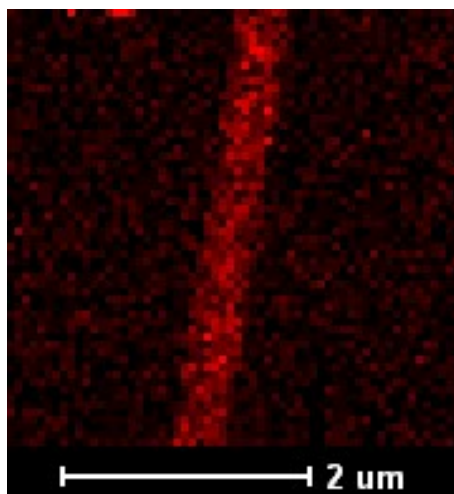
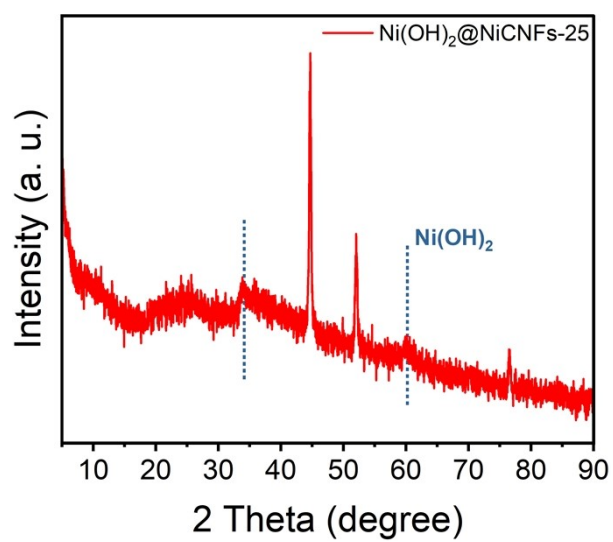**Fig. S4** EDX mapping of C element of Pt-Ni(OH)$_2$@Ni-CNFs-2.

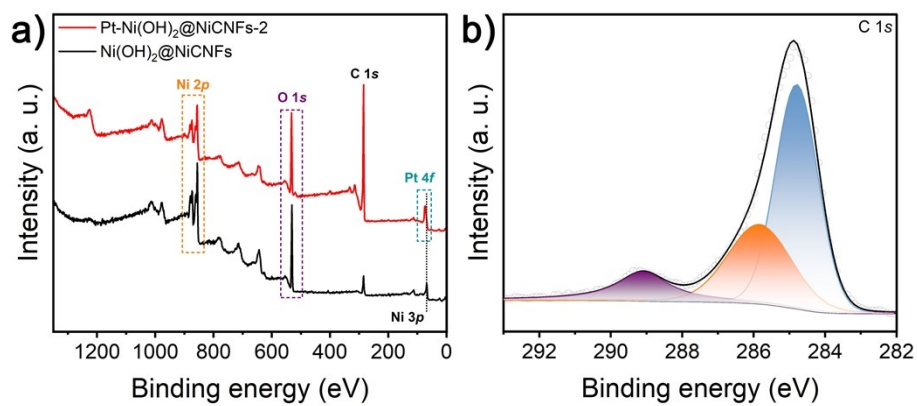**Fig. S5** XRD pattern of Ni(OH)$_2$@Ni-CNFs-25.

Fig. S6 (a) XPS full survey spectra of Pt-Ni(OH)$_2$@Ni-CNFs-2 and Ni(OH)$_2$@Ni-CNFs. (b) Narrow-scan XPS spectrum of C 1s of Pt-Ni(OH)$_2$@Ni-CNFs-2.
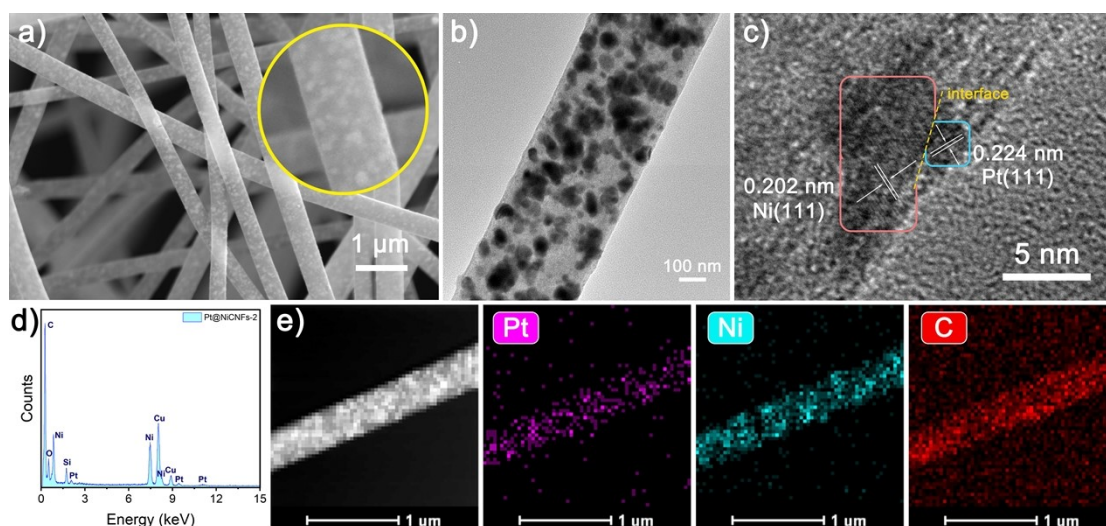
Fig. S7 (a) SEM image, (b) TEM image, (c) HRTEM image and (d) EDX pattern of Pt@Ni-CNFs-2. (e) HAADF-STEM micrograph and EDX mappings of Pt, Ni and C elements of Pt@Ni-CNFs-2.
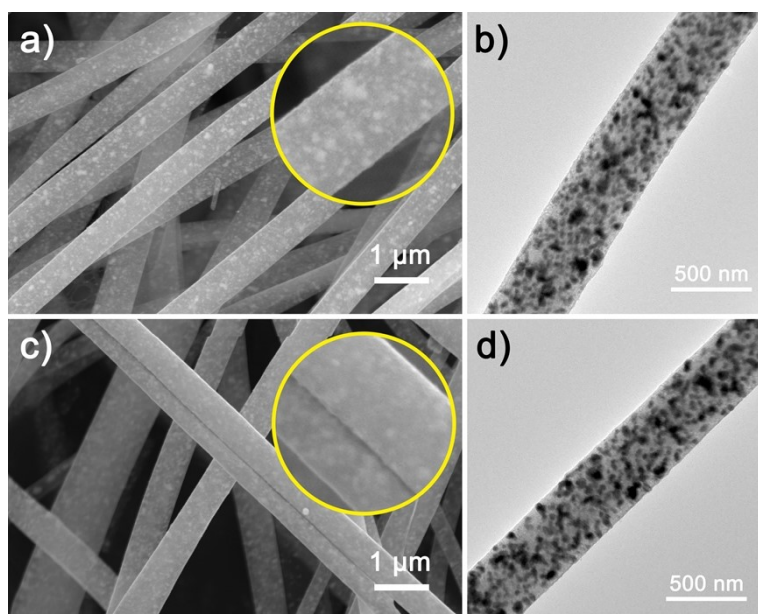
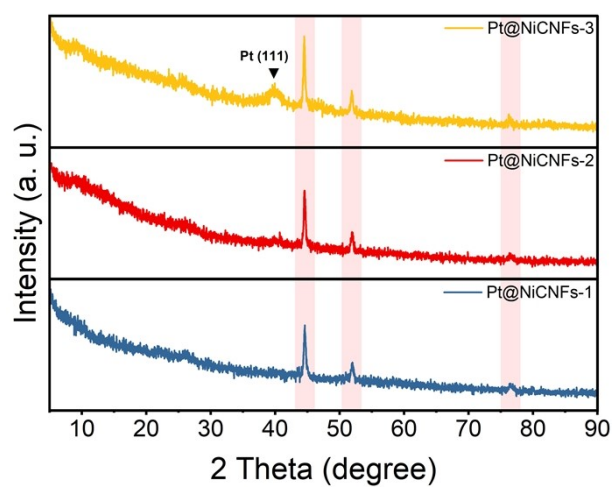**Fig. S8** SEM and TEM images of (a) and (b) Pt@Ni-CNFs-1, (c) and (d) Pt@Ni-CNFs-3.

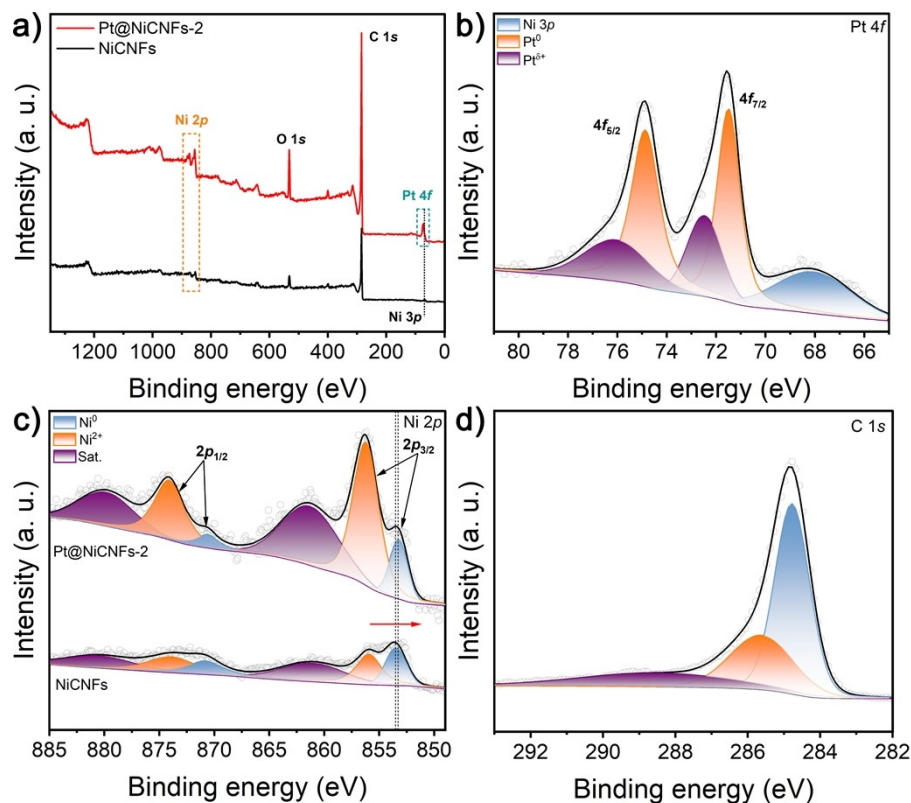**Fig. S9** XRD patterns of different samples.

Fig. S10 (a) XPS full survey spectra of Pt@Ni-CNFs-2 and Ni-CNFs. (b) Narrow-scan XPS spectrum of Pt 4f of Pt@Ni-CNFs-2. (c) Ni 2p spectra of Pt@Ni-CNFs-2 and Ni-CNFs. (d) C 1s spectrum of Pt@Ni-CNFs-2.
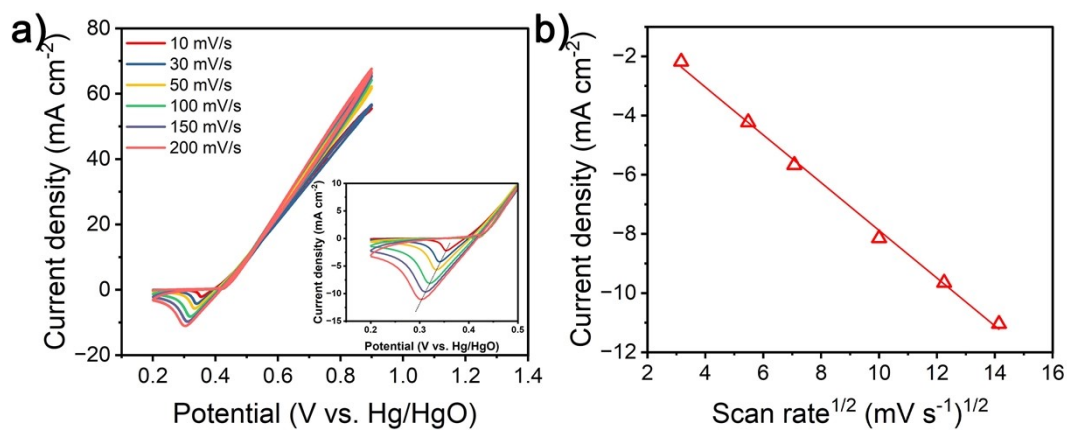
Fig. S11 (a) CV curves of Pt-Ni(OH)$_2$@Ni-CNFs-2 for UOR at different scan rates from 10 to 200 mV s^{-1} without iR-compensation. (b) Proportionality of the corresponding reduction peak current density of Ni^{2+}/Ni^{3+} redox reaction to the square roots of scan rates.

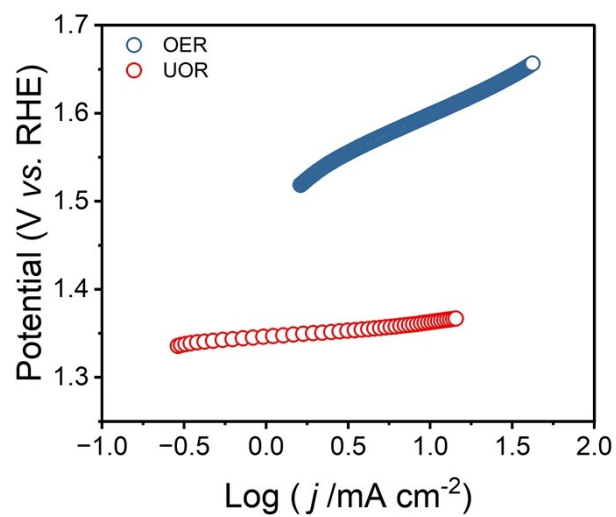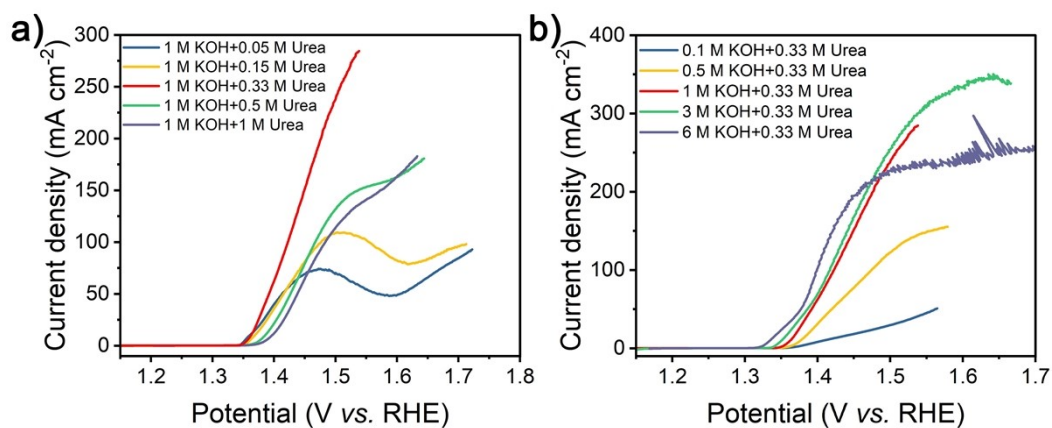**Fig. S12** Tafel plots of Pt-Ni(OH)$_2$@Ni-CNFs-2 for UOR and OER.

Fig. S13 Polarization curves of Pt-Ni(OH)$_2$@Ni-CNFs-2 for UOR in different electrolyte: (a) 1 M KOH with different concentrations of urea and (b) 0.33 M urea with different concentrations of KOH.
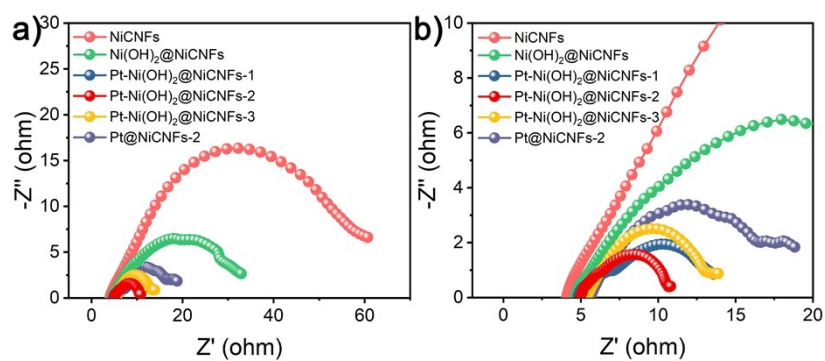
Fig. S14 (a) Nyquist plots of as-prepared catalysts at the potential of 0.5 V vs. Hg/HgO electrode. (b) Nyquist plots in a narrow range.
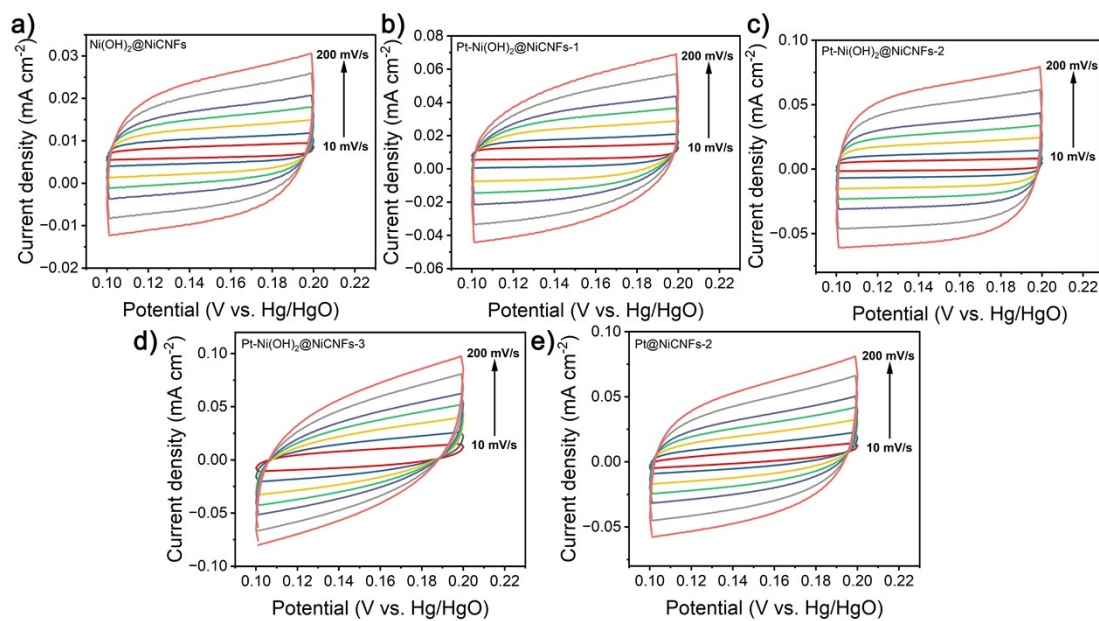
Fig. S15 CV curves of different catalysts in the 1 M KOH/0.33 M urea electrolyte with different scan rates from 10 to 200 mV s^{-1} in the region of 0.1-0.2 V vs. Hg/HgO: (a) Ni(OH)$_2$@Ni-CNFs, (b) Pt-Ni(OH)$_2$@Ni-CNFs-1, (c) Pt-Ni(OH)$_2$@Ni-CNFs-2, (d) Pt-Ni(OH)$_2$@Ni-CNFs-3 and (e) Pt@Ni-CNFs-2.
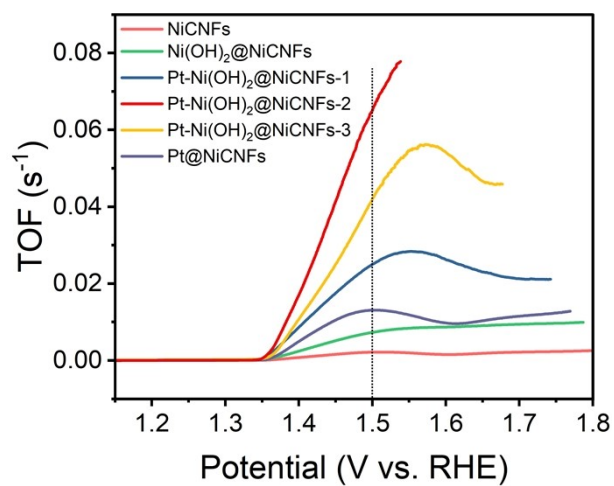
Fig. S16 TOF plots of different catalysts for UOR.
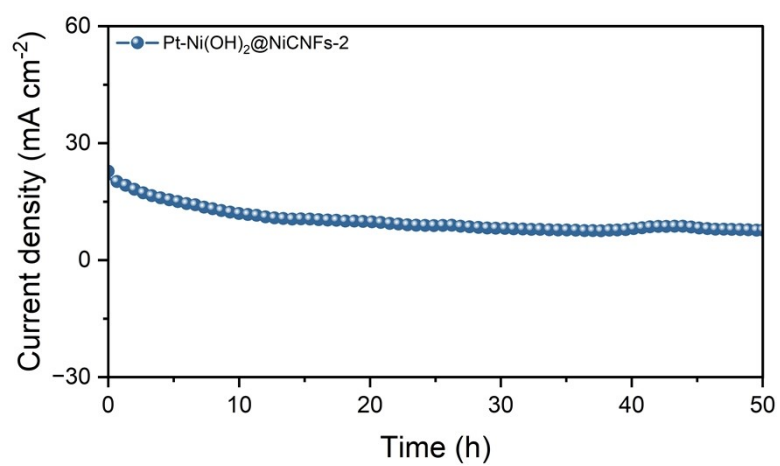
Fig. S17 i-t curve of Pt-Ni(OH)$_2$@Ni-CNFs-2 for UOR in 1 M KOH/0.33 M urea without replacing the electrolyte.
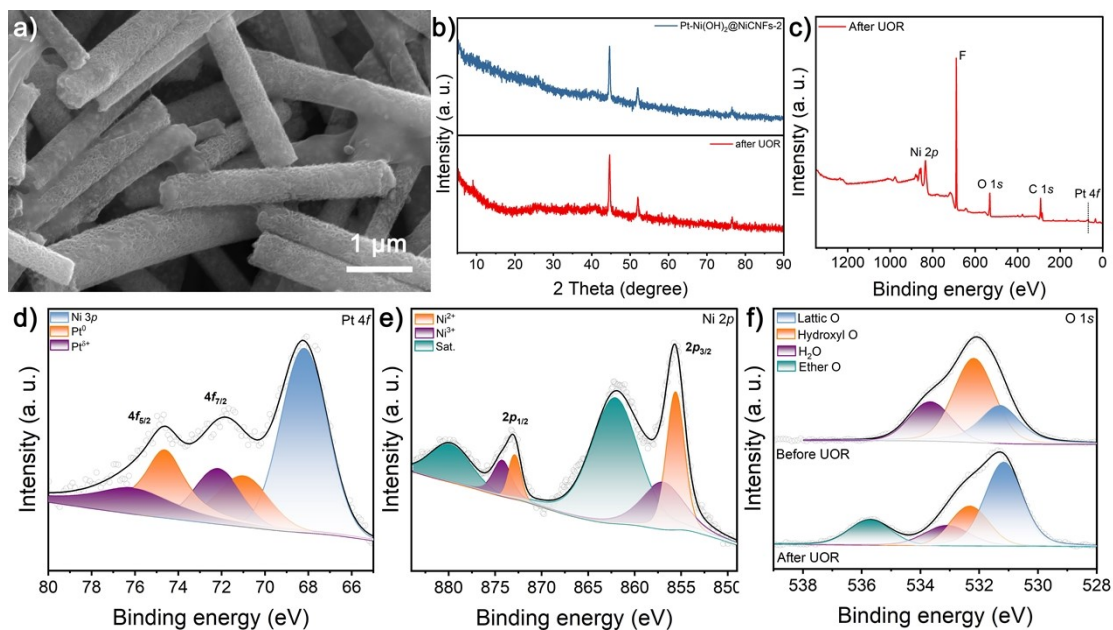
Fig. S18 (a) SEM image, (b) XRD patterns and (c-f) XPS spectra of Pt-Ni(OH)$_2$@Ni-CNFs-2 after UOR process.
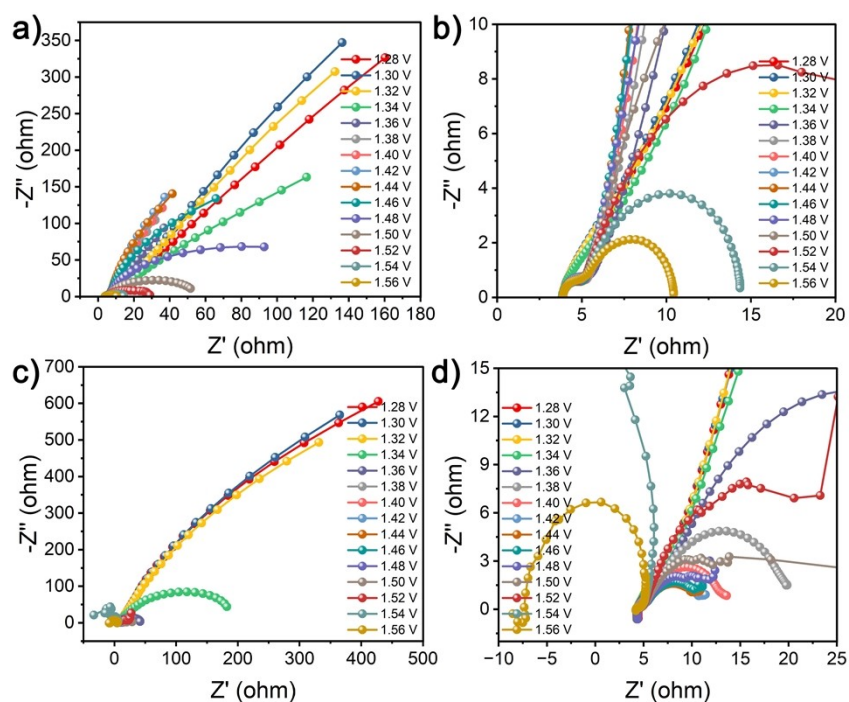
Fig. S19 Nyquist plots of Pt-Ni(OH)$_2$@Ni-CNFs-2 at different potentials for (a-b) OER and (c-d) UOR processes.
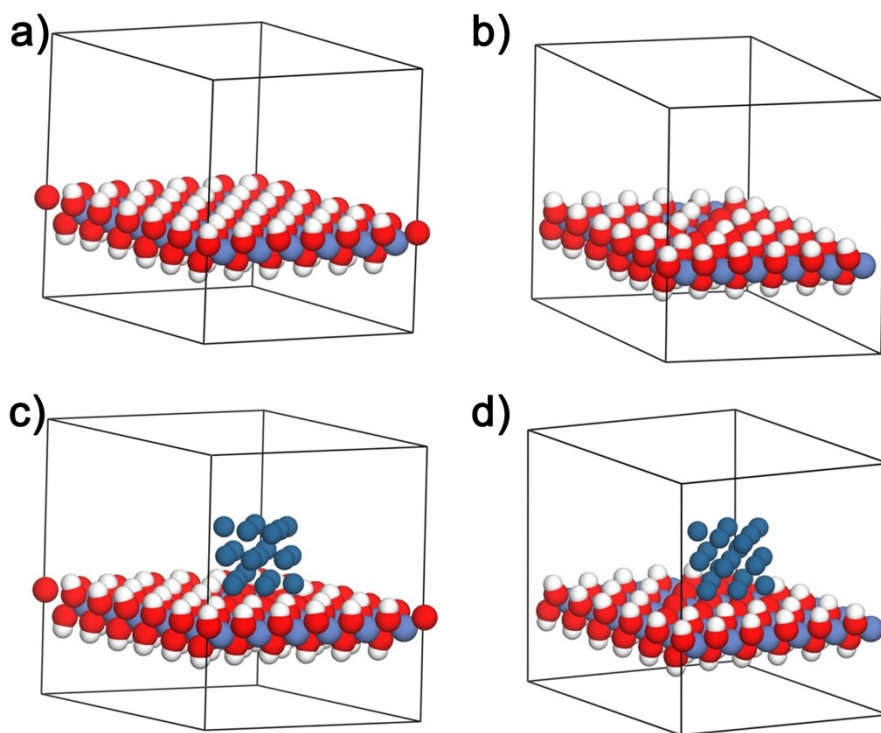
Fig. S20 Model structures of Ni(OH)$_2$ and Pt-Ni(OH)$_2$ catalysts during the dehydrogenation progress. Side view of (a-b) Ni(OH)$_2$ and (c-d) Pt-Ni(OH)$_2$.
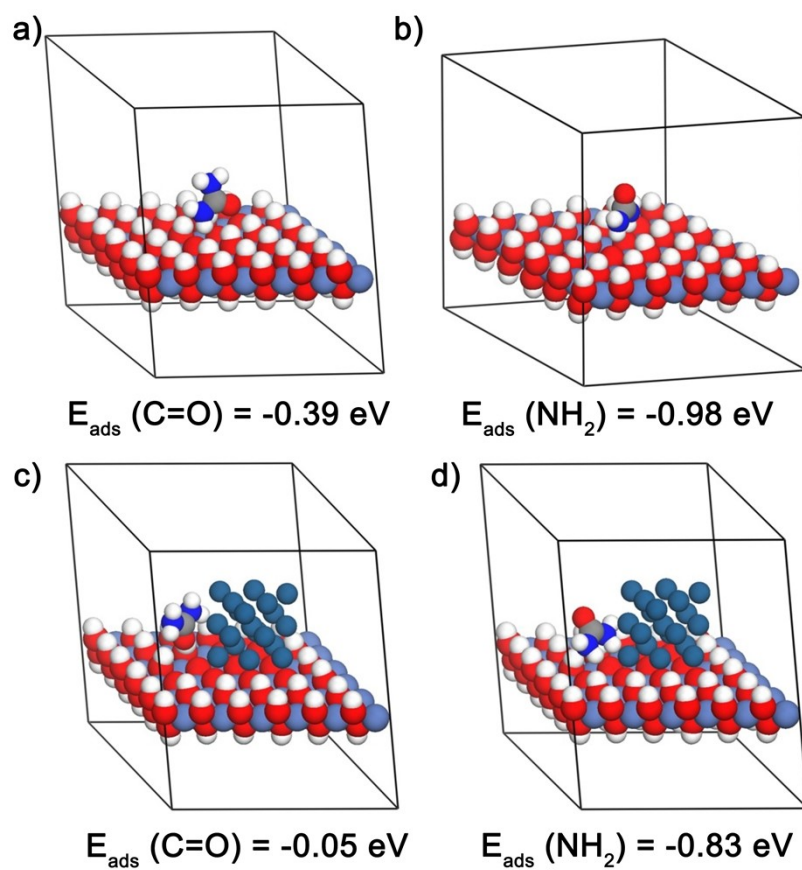
Fig. S21 Comparison of the adsorption energies of -NH$_2$ and -C=O groups in urea molecules adsorbed on the surface of (a-b) Ni(OH)$_2$ and (c-d) Pt-Ni(OH)$_2$ catalysts.
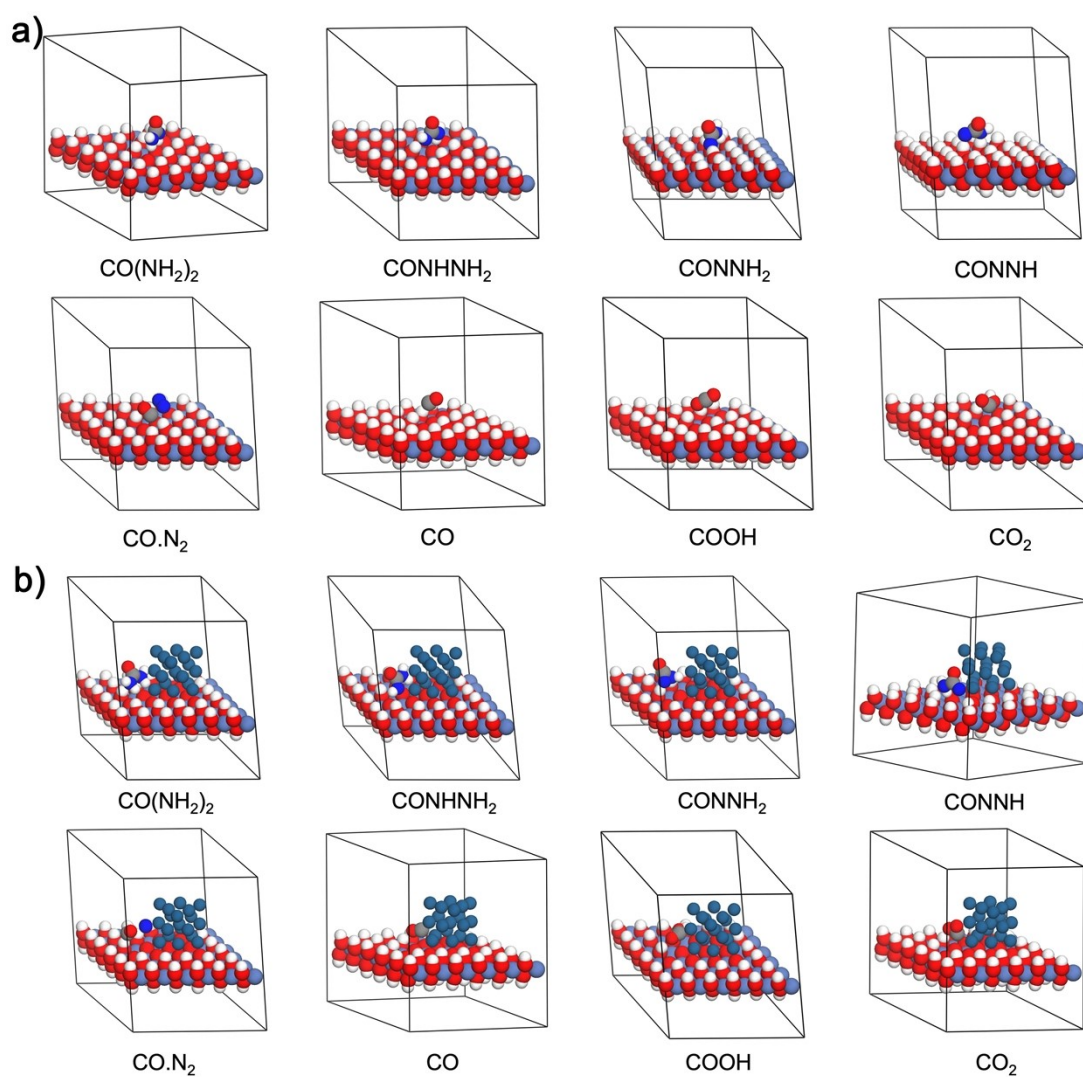
Fig. S22 Model structures of intermediates on the surface of (a) $Ni(OH)_2$ and (b) Pt-$Ni(OH)_2$ catalysts during the UOR process.
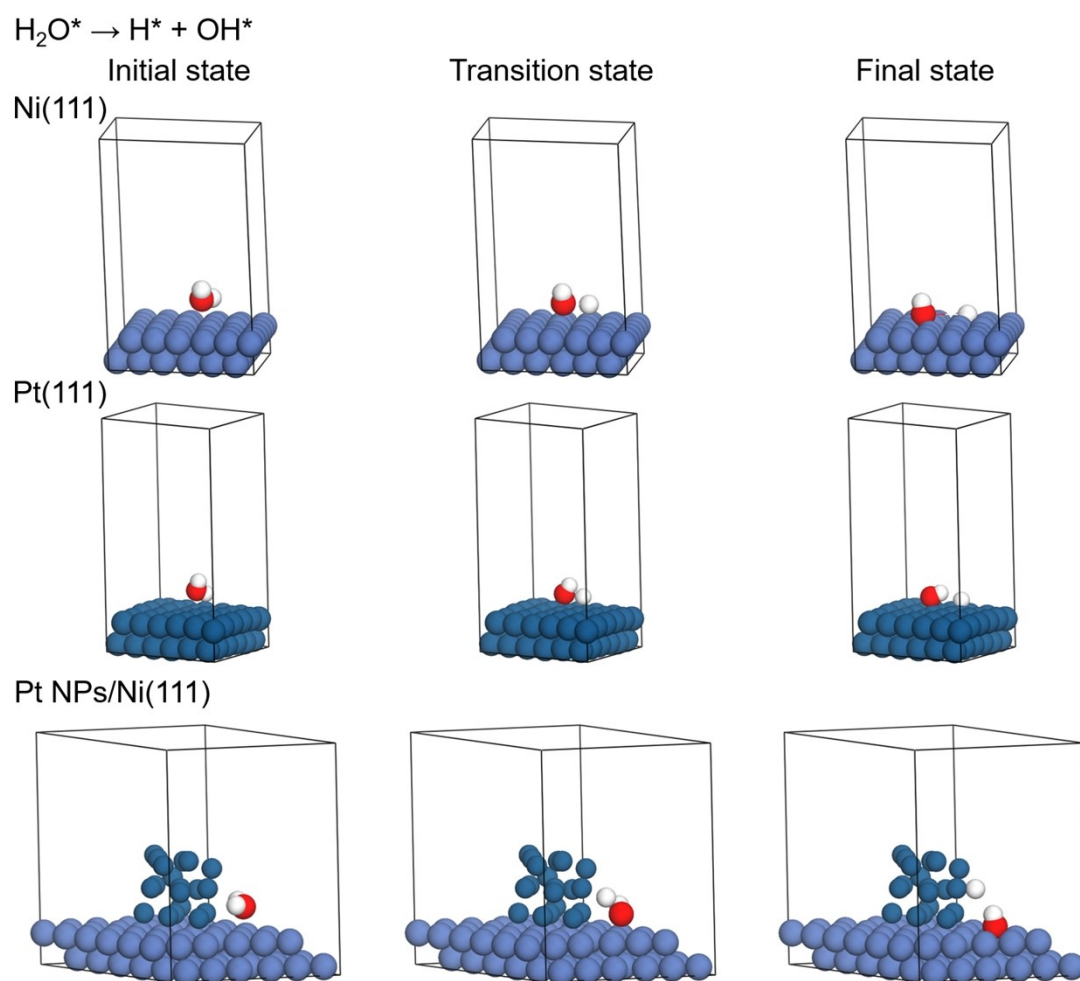
Fig. S23. DFT calculated models for activated H_2O to OH* and H* on the surface of Pt(111), Ni(111) and Pt NPs/Ni(111). Here, H, O, Ni and Pt atoms are indicated by white, red, cyan and dark blue spheres, respectively.
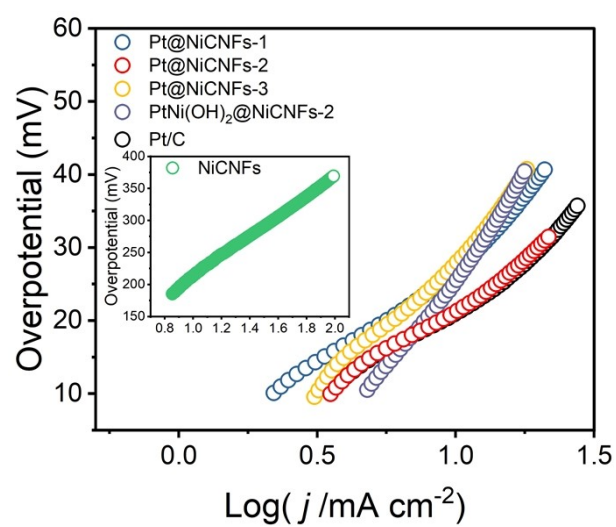
Fig. S24. Tafel plots of different catalysts.
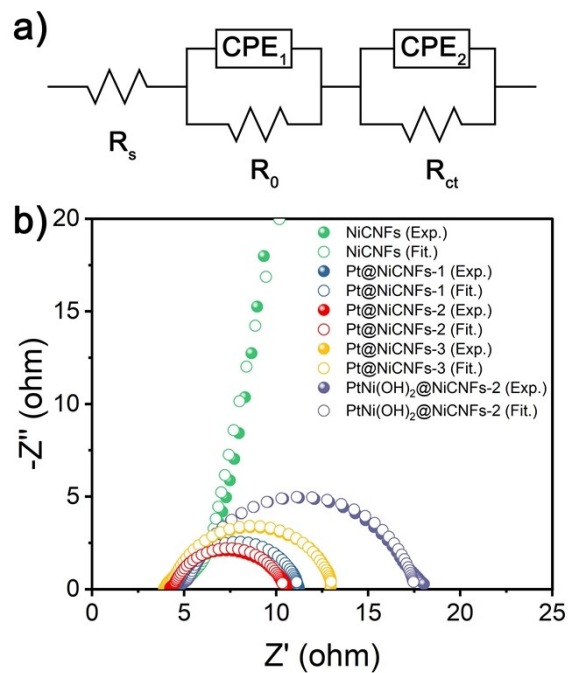
Fig. S25 (a) The equivalent circuit model of electrodes. R_s is the solution resistance, R_{ct} is the charge transfer resistance, R_0 is the contact resistance between the catalyst and electrode, CPE_1 and CPE_2 are the signs of the constant phase element and the double-layer capacitance, respectively. (b) Nyquist plots of different catalysts.
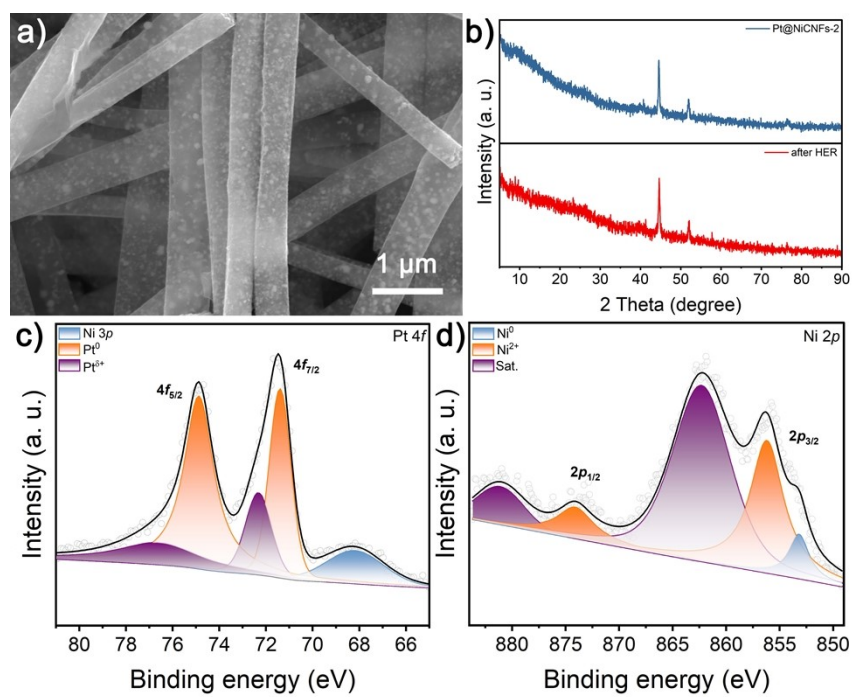
Fig. S26 (a) SEM image, (b) XRD patterns, and XPS spectra of (c) Pt 4f and (d) Ni 2p of Pt@Ni-CNFs-2 after HER process.
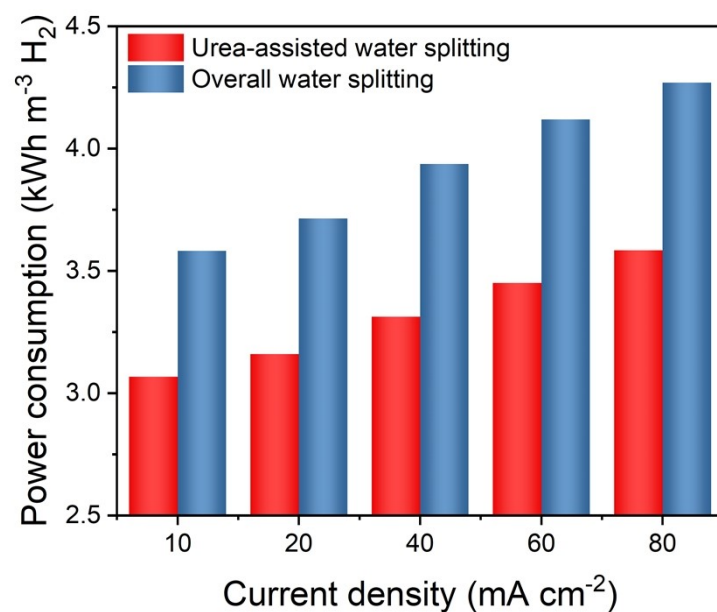
Fig. S27 Comparison of power consumption at different current densities for hydrogen production in the urea-assisted water splitting and overall water splitting systems.
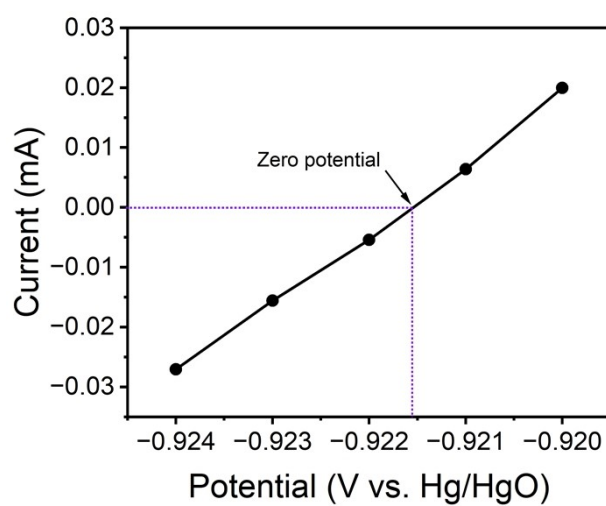
Fig. S28 The current as a function of the applied potentials for the calibration of Hg/HgO reference electrode.

Table S1 Mass loading of Pt and Ni elements in different samples.

Sample	Pt (wt%)	Ni (wt%)
Ni-CNFs	NA	46.1
Ni(OH)$_2$@Ni-CNFs	NA	38.2
Pt-Ni(OH)$_2$@Ni-CNFs-1	2.2	38.3
Pt-Ni(OH)$_2$@Ni-CNFs-2	6.1	35.3
Pt-Ni(OH)$_2$@Ni-CNFs-3	8.8	34.8
Pt@Ni-CNFs-1	2.9	32.7
Pt@Ni-CNFs-2	6.5	34.3
Pt@Ni-CNFs-3	10.8	29.5

Table S2 Comparison of C_{dl}, ECSA and RF values of different prepared samples.

Catalyst	C_{dl} (mA cm^{-2})	ECSA (cm^2)	RF
Ni(OH)$_2$@Ni-CNFs	0.08	0.4	2
Pt-Ni(OH)$_2$@Ni-CNFs-1	0.21	1.05	5.25
Pt-Ni(OH)$_2$@Ni-CNFs-2	0.3	1.5	7.5
Pt-Ni(OH)$_2$@Ni-CNFs-3	0.25	1.25	6.25
Pt@Ni-CNFs-2	0.24	1.2	6

Table S3 Comparison of some representative catalysts for UOR properties.

Catalyst	Mass loading (mg cm^{-2})	Electrolyte (1 M KOH)	j (mA cm^{-2})	Potential (V *vs.* RHE)	Tafel slope (mV dec^{-1})
Pt-Ni(OH)$_2$ @Ni-CNFs-2	1	0.33 M urea	10	1.363	13.7
			50	1.391	
			100	1.422	
β-Ni(OH)$_2$[8]	0.2	0.5 M urea	10	~1.56	NA
V-doped Ni(OH)$_2$/NF[6]	NA	0.33 M urea	100	1.47	29.1
Fe-Ni$_3$S$_2$@FeNi$_3$-8[9]	NA	0.33 M urea	10	1.4	29
Ni(OH)$_2$/NF[10]	10	0.33 M urea	100	~1.45	NA
CoW-500-Ni[11]	NA	0.3 M urea	50	1.41	NA
NiFe-MIL-53-NH$_2$[12]	0.15	0.33 M urea	50	1.398	14
NF/NiMoO-Ar[13]	NA	0.5 M urea	10	1.37	19
Ni@NCT-3[14]	0.285	0.5 M urea	10	1.38	76.3
NiS@Ni-CNFs[15]	2	0.33 M	10	1.366	12.5
NiS@Ni$_3$S$_2$[16]	0.0312	0.5 M urea	10	1.37	40
L-MnO$_2$[17]	1.5	0.5 M urea	10	1.37	89
Ni(OH)$_2$-PBA[18]	NA	0.5 M urea	10	1.38	80
NiFe LDH @Ni(OH)$_2$-z[19]	NA	0.5 M urea	100	1.44	37
Ni(OH)$_2$ @ Ni$_2$Fe$_2$/NF-60[20]	NA	0.5 M urea	100	1.44	53
NiTe$_2$/Ni(OH)$_2$/ CFC[21]	NA	0.33 M urea	73	1.523	NA

Table S4 Comparison of some representative catalysts for HER properties in 1 M KOH.

Catalyst	Mass loading (mg cm^{-2})	j (mA cm^{-2})	Overpotential (mV)	Tafel slope (mV dec^{-1})
Pt@Ni-CNFs-2	1	10	20.8	20.1
		50	49.9	
		200	107.8	
Pt$_{SA}$-NiO[22]	NA	10	55	36
Ir CSs/PHCNBs[23]	0.114	10	35	23.07
		50	70	
Pt@Co-Mo$_2$S$_4$-NGNF[24]	4	10	27	32
		200	119	
Pt-NiS@Ni-CNFs[15]	2	10	62.6	42.8
Pt-MoAl$_{1-x}$B[25]	NA	10	32	83.6
PtMo-NC[26]	0.038	10	35	32
Pt$_3$Fe/NMCS-A[27]	0.412	10	29	50
Pt/LiCoO$_2$[28]	0.204	10	61	39.5
gr-Pt/Mo$_2$C[29]	0.278	10	36.5	34.3
PtSi[30]	0.34	10	38	81
N,Pt-MoS$_2$[31]	NA	10	38	39
Pt$_{SA}$-NiO/Ni[32]	NA	10	26	27.07
Pt$_3$Co@NCNT[33]	0.4	10	36	34.8
Pt@CoS$_2$-NrGO[34]	0.1	10	39	35
Pt-CoS$_2$/CC[35]	NA	10	24	82
PtNi-O/C[36]	0.0051	10	39.8	78.8
Pt/Nb-Co(OH)$_2$[37]	0.283	10	112	82
Pt-NiFe LDH-ht/CC[38]	0.205	10	101	127
		50	205	
Pt$_1$-Mo$_2$C-C[39]	0.2	10	155	64

Pt/Ni-PCNFs-50[40]	0.408	10	46	43.8

Table S5 Comparison of some representative catalysts for urea-assisted water splitting.

Electrolyzer [Anode‖Cathode]	Electrolyte (1 M KOH)	j (mA cm^{-2})	Voltage (V)	Ref.
Pt-Ni(OH)$_2$@Ni-CNFs-2 ‖Pt@Ni-CNFs-2	0.33 M urea	10	1.40	This work
Mo-NiS	0.5 M urea	10	1.51	[41]
N-NiS/NiS$_2$	0.33 M urea	10	1.62	[42]
Pt-NiS@Ni-CNFs	0.33 M urea	10	1.44	[15]
NiS/MoS$_2$@CC	0.5 M urea	10	1.46	[43]
Ni@NCNT-3	0.5 M urea	10	1.56	[14]
NiFe-MIL-53-NH$_2$	0.33 M urea	10	1.566	[12]
Fe-Ni$_3$S$_2$@FeNi$_3$-8	0.33 M urea	10	1.50	[9]
NiCo$_2$S$_4$/CC	0.33 M urea	10	1.45	[44]
Ni$_4$N/Cu$_3$N/CF	0.5 M urea	10	1.48	[45]
Ni-MOF-0.5/NF	0.5 M urea	10	1.52	[46]
Ni$_3$S$_2$-Ni$_3$P/NF-2	0.5 M urea	10	1.43	[47]
NF/CNNH-20	0.5 M urea	10	1.43	[48]
Ni(OH)$_2$-NiMoO$_x$/NF	0.5 M urea	10	1.42	[49]
MNPBA-P	0.5 M urea	10	1.5	[18]
NiFeCo LDH/NF	0.33 M urea	10	1.49	[50]
CoNiFeS-OH	0.33 M urea	10	1.461	[51]
HC-NiMoS/Ti	0.5 M urea	10	1.59	[52]
H-NiFe-LDH/NF	0.33 M urea	10	1.418	[53]
NC-FNCP	0.5 M urea	10	1.52	[54]
FQD/CoNi-LDH/NF	0.5 M urea	10	1.45	[55]

References

1 H. Ju, S. Badwal and S. Giddey, *Appl. Energy*, 2018, **231**, 502-533.

2 Z. Chen, Y. Xu, D. Ding, G. Song, X. Gan, H. Li, W. Wei, J. Chen, Z. Li, Z. Gong, X. Dong, C. Zhu, N. Yang, J. Ma, R. Gao, D. Luo, S. Cong, L. Wang, Z. Zhao and Y. Cui, *Nat. Commun.*, 2022, **13**, 763.

3 J. P. Perdew, K. Burke and M. Ernzerhof, *Phys. Rev. Lett.*, 1996, **77**, 3865-3868.

4 J. P. Perdew, M. Ernzerhof and K. Burke, *J. Chem. Phys.*, 1996, **105**, 9982-9985.

5 L. Zhang, L. Wang, H. Lin, Y. Liu, J. Ye, Y. Wen, A. Chen, L. Wang, F. Ni, Z. Zhou, S. Sun, Y. Li, B. Zhang and H. Peng, *Angew. Chem. Int. Ed.*, 2019, **58**, 16820 –16825.

6 H. Qin, Y. Ye, J. Li, W. Jia, S. Zheng, X. Cao, G. Lin and L. Jiao, *Adv. Funct. Mater.*, 2023, **33**, 2209698.

7 Y. Liao, Y. Chen, L. Li, S. Luo, Y. Qing, C. Tian, H. Xu, J. Zhang and Y. Wu, *Adv. Funct. Mater.*, 2023, **33**, 2303300.

8 W. Chen, L. Xu, X. Zhu, Y. C. Huang, W. Zhou, D. Wang, Y. Zhou, S. Du, Q. Li, C. Xie, L. Tao, C. L. Dong, J. Liu, Y. Wang, R. Chen, H. Su, C. Chen, Y. Zou, Y. Li, Q. Liu and S. Wang, *Angew. Chem. Int. Ed.*, 2021, **60**, 7297-7307.

9 W. Zhang, Q. Jia, H. Liang, L. Cui, D. Wei and J. Liu, *Chem. Eng. J.*, 2020, **396**, 125315.

10 S. W. Tatarchuk, J. J. Medvedev, F. Li, Y. Tobolovskaya and A. Klinkova, *Angew. Chem. Int. Ed.*, 2022, **61**, e202209839.

11 R. Li, H. Xu, P. Yang, D. Wang, Y. Li, L. Xiao, X. Lu, B. Wang, J. Zhang and M. An, *Nano-Micro Lett.*, 2021, **13**, 120.

12 Z. Gao, Y. Wang, L. Xu, Q. Tao, X. Wang, Z. Zhou, Y. Luo, J. Yu and Y. Huang, *Chem. Eng. J.*, 2022, **433**, 133515.

13 Z.-Y. Yu, C.-C. Lang, M.-R. Gao, Y. Chen, Q.-Q. Fu, Y. Duan and S.-H. Yu, *Energy Environ. Sci.*, 2018, **11**, 1890-1897.

14 Q. Zhang, F. M. D. Kazim, S. Ma, K. Qu, M. Li, Y. Wang, H. Hu, W. Cai and Z. Yang, *Appl. Catal. B-Environ.*, 2021, **280**, 119436.

15 M. Zhong, J. Yang, M. Xu, S. Ren, X. Chen, C. Wang, M. Gao and X. Lu, *Small*,

2023, DOI: 10.1002/smll.202304782, 2304782.

16   L. Sha, T. Liu, K. Ye, K. Zhu, J. Yan, J. Yin, G. Wang and D. Cao, *J. Mater. Chem. A*, 2020, **8**, 18055-18063.

17   S. Chen, J. Duan, A. Vasileff and S. Z. Qiao, *Angew. Chem. Int. Ed.*, 2016, **55**, 3804-3808.

18   H. Xu, K. Ye, K. Zhu, Y. Gao, J. Yin, J. Yan, G. Wang and D. Cao, *ACS Sustain. Chem. Eng.*, 2020, **8**, 16037-16045.

19   Y. Ye, Y. Gan, R. Cai, X. Dai, X. Yin, F. Nie, Z. Ren, B. Wu, Y. Cao and X. Zhang, *J. Alloy. Compd.*, 2022, **921**, 166145.

20   L. Zhang, T. Wang, H. Wu, H. Wang and F. Wang, *J. Alloy. Compd.*, 2022, **918**, 165564.

21   B. Xu, X. Yang, X. Liu, W. Song, Y. Sun, Q. Liu, H. Yang and C. Li, *J. Power Sources*, 2020, **449**, 227585.

22   Y. Da, Z. Tian, R. Jiang, G. Chen, Y. Liu, Y. Xiao, J. Zhang, S. Xi, W. Chen, X. Han and W. Hu, *ACS Nano*, 2023, **17**, 18539−18547.

23   Y. Zhao, Q. Sun, X. Zhou, Z. Duan, C. Zhang, G. R. Xu, D. Ju and L. Wang, *Small*, 2023, DOI: 10.1002/smll.202305343, 2305343.

24   S. Vijayapradeep, N. Logeshwaran, S. Ramakrishnan, A. Rhan Kim, P. Sampath, D. Hwan Kim and D. Jin Yoo, *Chem. Eng. J.*, 2023, **473**, 145348.

25   S. J. Park, T. H. Nguyen, D. T. Tran, V. A. Dinh, J. H. Lee and N. H. Kim, *Energy Environ. Sci.*, 2023, **16**, 4093-4104.

26   H. Zhang, F. Wan, X. Li, X. Chen, S. Xiong and B. Xi, *Adv. Funct. Mater.*, 2023, **33**, 2306340.

27   P. Kuang, Z. Ni, B. Zhu, Y. Lin and J. Yu, *Adv. Mater.*, 2023, **35**, 2303030.

28   X. Zheng, P. Cui, Y. Qian, G. Zhao, X. Zheng, X. Xu, Z. Cheng, Y. Liu, S. X. Dou and W. Sun, *Angew. Chem. Int. Ed.*, 2020, **59**, 14533-14540.

29   Z. Liu, J. Li, S. Xue, S. Zhou, K. Qu, Y. Li and W. Cai, *J. Energy Chem.*, 2020, **47**, 317-323.

30   Z. Pu, T. Liu, G. Zhang, Z. Chen, D.-S. Li, N. Chen, W. Chen, Z. Chen and S. Sun, *Adv. Energy Mater.*, 2022, **12**, 2200293.

31   Y. Sun, Y. Zang, W. Tian, X. Yu, J. Qi, L. Chen, X. Liu and H. Qiu, *Energy Environ. Sci.*, 2022, **15**, 1201-1210.

32   K. L. Zhou, Z. Wang, C. B. Han, X. Ke, C. Wang, Y. Jin, Q. Zhang, J. Liu, H. Wang and H. Yan, *Nat. Commun.*, 2021, **12**, 3783.

33   S. L. Zhang, X. F. Lu, Z. P. Wu, D. Luan and X. W. D. Lou, *Angew. Chem. Int. Ed.*, 2021, **60**, 19068-19073.

34   N. Logeshwaran, S. Ramakrishnan, S. S. Chandrasekaran, M. Vinothkannan, A. R. Kim, S. Sengodan, D. B. Velusamy, P. Varadhan, J.-H. He and D. J. Yoo, *Appl. Catal. B-Environ.*, 2021, **297**, 120405.

35   X. Han, X. Wu, Y. Deng, J. Liu, J. Lu, C. Zhong and W. Hu, *Adv. Energy Mater.*, 2018, **8**, 1800935.

36   Z. Zhao, H. Liu, W. Gao, W. Xue, Z. Liu, J. Huang, X. Pan and Y. Huang, *J. Am. Chem. Soc.*, 2018, **140**, 9046-9050.

37   Y. Tian, M. Wen, A. Huang, Q. Wu, Z. Wang, Q. Zhu, T. Zhou and Y. Fu, *Small*, 2023, **19**, 2207569.

38   S. Anantharaj, K. Karthick, M. Venkatesh, T. V. S. V. Simha, A. S. Salunke, L. Ma, H. Liang and S. Kundu, *Nano Energy*, 2017, **39**, 30-43.

39   S. Niu, J. Yang, H. Qi, Y. Su, Z. Wang, J. Qiu, A. Wang and T. Zhang, *J. Energy Chem.*, 2021, **57**, 371-377.

40   J. Xu, M. Zhong, N. Song, C. Wang and X. Lu, *Chin. Chem. Lett.*, 2023, **34**, 107359.

41   Z. Yue, W. Yanmin, K. Deqiang, Z. Qianqian, Z. Lei, Z. Jialin, C. Xuemin, L. Yanan, X. Yan and M. Chao, *Adv. Funct. Mater.*, 2022, **33**, 2210656.

42   H. Liu, Z. Liu, F. Wang and L. Feng, *Chem. Eng. J.*, 2020, **397**, 125507.

43   C. Gu, G. Zhou, J. Yang, H. Pang, M. Zhang, Q. Zhao, X. Gu, S. Tian, J. Zhang, L. Xu and Y. Tang, *Chem. Eng. J.*, 2022, **443**, 136321.

44   W. Song, M. Xu, X. Teng, Y. Niu, S. Gong, X. Liu, X. He and Z. Chen, *Nanoscale*, 2021, **13**, 1680-1688.

45   J. Li, C. Yao, X. Kong, Z. Li, M. Jiang, F. Zhang and X. Lei, *ACS Sustain. Chem. Eng.*, 2019, **7**, 13278-13285.

46   S. Zheng, Y. Zheng, H. Xue and H. Pang, *Chem. Eng. J.*, 2020, **395**, 125166.

47   J. Liu, Y. Wang, Y. Liao, C. Wu, Y. Yan, H. Xie and Y. Chen, *ACS Appl. Mater. Interfaces*, 2021, **13**, 26948-26959.

48   Y. Cheng, F. Liao, H. Dong, H. Wei, H. Geng and M. Shao, *J. Power Sources*, 2020, **480**, 229151.

49   Z. Dong, F. Lin, Y. Yao and L. Jiao, *Adv. Energy Mater.*, 2019, **9**, 1902703.

50   P. Babar, A. Lokhande, V. Karade, B. Pawar, M. G. Gang, S. Pawar and J. H. Kim, *ACS Sustain. Chem. Eng.*, 2019, **7**, 10035-10043.

51   C. Fang, D. Zhang, X. Wang and R. Li, *Inorg. Chem. Front.*, 2022, **9**, 3643-3653.

52   X. Wang, J. Wang, X. Sun, S. Wei, L. Cui, W. Yang and J. Liu, *Nano Res.*, 2017, **11**, 988-996.

53   L. Chen, H. Wang, L. Tan, D. Qiao, X. Liu, Y. Wen, W. Hou and T. Zhan, *J. Colloid Interface Sci.*, 2022, **618**, 141-148.

54   J. Zhang, S. Huang, P. Ning, P. Xin, Z. Chen, Q. Wang, K. Uvdal and Z. Hu, *Nano Res.*, 2021, **15**, 1916-1925.

55   Y. Feng, X. Wang, J. Huang, P. Dong, J. Ji, J. Li, L. Cao, L. Feng, P. Jin and C. Wang, *Chem. Eng. J.*, 2020, **390**, 124525.